PNAS RESEARCH ARTICLE | APPLIED PHYSICAL SCIENCES OPEN ACCESS

Label-free drug interaction screening via Raman microscopy

Narangerel Altangerel[a], Benjamin W. Neuman[a], Philip R. Hemmer[a], Vladislav V. Yakovlev[a], Navid Rajil[a], Zhenhuan Yi[a], Alexei V. Sokolov[a], and Marlan O. Scully[a,b,c,1]

Contributed by Marlan O. Scully; received March 14, 2023; accepted May 11, 2023; reviewed by Randy A. Bartels and Zhiwen Liu

Development of a simple, label-free screening technique capable of precisely and directly sensing interaction-in-solution over a size range from small molecules to large proteins such as antibodies could offer an important tool for researchers and pharmaceutical companies in the field of drug development. In this work, we present a thermostable Raman interaction profiling (TRIP) technique that facilitates low-concentration and low-dose screening of binding between protein and ligand in physiologically relevant conditions. TRIP was applied to eight protein–ligand systems, and produced reproducible high-resolution Raman measurements, which were analyzed by principal component analysis. TRIP was able to resolve time-depending binding between 2,4-dinitrophenol and transthyretin, and analyze biologically relevant SARS-CoV-2 spike-antibody interactions. Mixtures of the spike receptor–binding domain with neutralizing, nonbinding, or binding but nonneutralizing antibodies revealed distinct and reproducible Raman signals. TRIP holds promise for the future developments of high-throughput drug screening and real-time binding measurements between protein and drug.

Raman spectroscopy | aqueous Raman sampling | protein–ligand interactions | protein–protein interactions

Significance

Proteins are the machinery of life, and their function is controlled by interactions: with cofactors, substrates, and proteins that sterically or conformationally modulate activity. We present a thermostable Raman interaction profiling (TRIP) technique that facilitates low-concentration and low-dose screening of binding between protein and ligand in physiologically relevant conditions. The proposed method can be used over a large variety of molecules ranging from small molecules to large proteins such as antibodies and offers an essential tool for researchers and pharmaceutical companies in the field of drug development. The TRIP holds the promise for future developments of high-throughput drug screening and real-time binding measurements between protein and drug.

Understanding molecular interactions and binding dynamics is important for developing and screening for new drugs (1, 2), understanding their efficiency (3), developing new biological probes for sensing and imaging (4) and fundamental understanding of enzymatic interactions (5). Recent advances in G-protein-coupled receptor (GPCR) inhibitors (6), antivirals (7), and anticancer therapeutics (8) demonstrate the power of alternative techniques to limit interactions. In particular, steric inhibitors can be used in place of the more-common enzyme inhibition techniques. However, traditional drug screening tends to focus on modulating enzyme activity, in part because it is more tractable for the assays (9). Therefore, there is an urgent need for a screening technique that directly measures molecular interactions without relying on any other readouts that are likely to be very sensitive to experimental conditions.

Here, we introduce a label-free direct screening approach, which measures bindings between protein and ligand in their physiologically relevant conditions. The proposed method, which is validated in this report, relies on Raman microscopic measurements from cooled sample solutions and, thus, is termed thermostable Raman interaction profiling (TRIP) to reflect on its distinct nature as compared to previous efforts. Raman microscopy is a label-free, chemically specific sensing and imaging tool, which requires no sample preparation and enables the analyses of aqueous samples in a relatively short acquisition time. It can detect minute changes in molecular geometry, particularly, the conformational transitions characteristic of biological macromolecules. These can create frequency shifts/intensity changes in Raman bands that aid the technique in the determination of protein structure, side-chain configuration, and observation of interacting side-chain groups (10). Since molecular geometry and force fields are sensitive to interactions between molecules, this allows the Raman spectroscopy method to investigate intermolecular interactions, including the formation of biologically important protein complexes and, potentially, detect subtle changes in vibrational plasticity associated with antigen–antibody (11) and protein–drug (12) interactions.

Raman spectroscopic techniques have been used to study intermolecular interactions and characteristics of proteins and nucleic acids (13), and Raman spectroscopy has been applied extensively as a structural probe for proteins (14, 15). However, these previous Raman studies lacked statistical representation and reproducibility of their Raman spectra. Fortunately, our technique is successfully applied to eight protein–ligand systems and shows exceptional reproducibility of the Raman measurements for each system. Its broad range of applicability is shown in the following workflow of the technique (Fig. 1). TRIP requires only a 10 μL droplet of 1 to 3 mg/mL protein concentration of phosphate-buffered saline (PBS) solution on a cooled gold-coated glass slide. The thin gold layer serves double purposes

Author contributions: N.A., B.W.N., P.R.H., and M.O.S. developed the concept of the study; N.A. designed research; N.A. performed research; N.A. analyzed data; and N.A., B.W.N., P.R.H., V.V.Y., N.R., Z.Y., A.V.S., and M.O.S. wrote the paper.

Reviewers: R.A.B., Colorado State University; and Z.L., Pennsylvania State University.

Competing interest statement: We are submitting a patent disclosure for the TRIP technique used in the paper.

[1]To whom correspondence may be addressed. Email: scully@tamu.edu.

Published July 18, 2023.

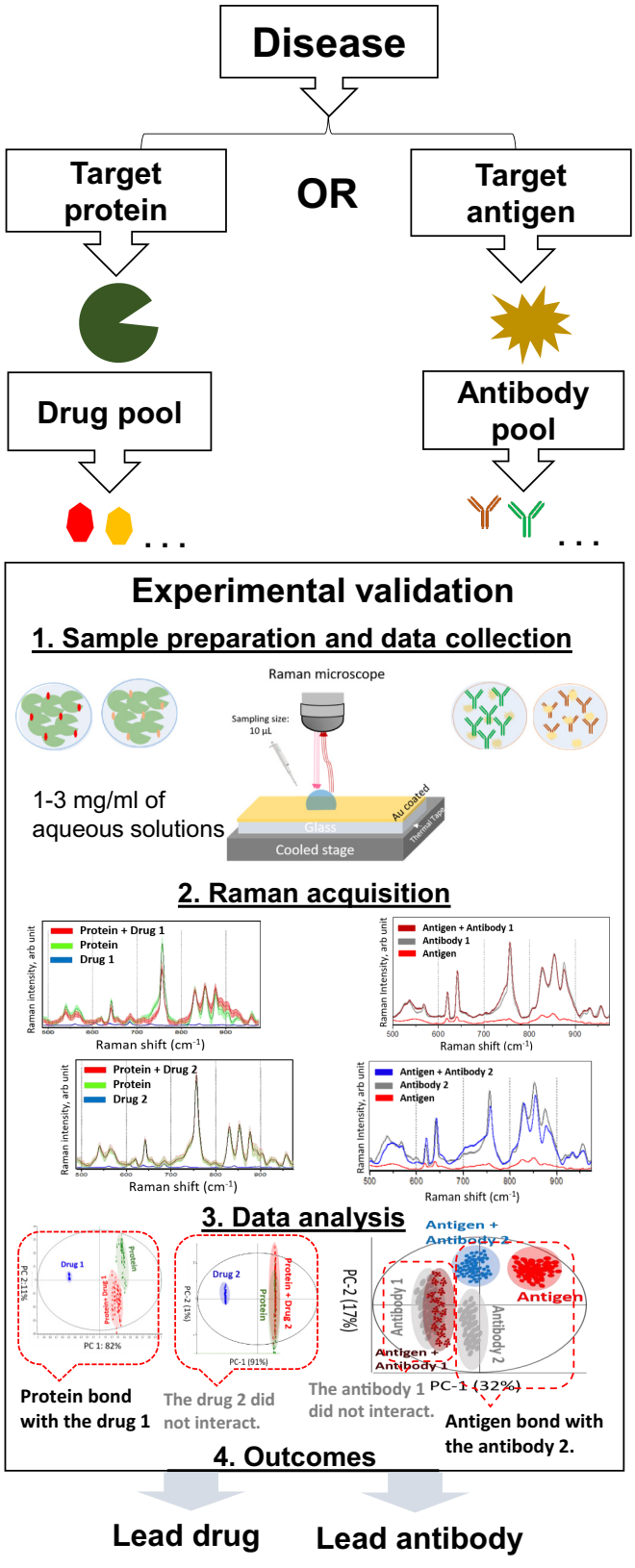

Fig. 1. The workflow of TRIP technique.

for dissipating thermal energy from the excitation laser and for blocking the fluorescent background from the glass slide. Our technique is used to detect binding-induced vibrational spectral changes in protein solutions, with and without ligand, using principal component analysis (PCA). By identifying key Raman bands that lead to the PCA separation, we can correlate spectral peaks to specific binding interactions between proteins and ligands.

Currently, there are some label-free techniques to study protein–ligand binding interactions in solution. Most label-free methods immobilize one biomolecule on a sensor surface and use an optical signal to detect a binding partner from solution as it associates with the immobilized biomolecules, such as surface plasmon resonance (SPR) (16), interferometry (17), and surface-enhanced Raman spectroscopy (SERS) (18). X-ray/neutron scattering is a nonoptical label-free technique (19), but interpreting of the raw measurements requires heavy modeling/processing and obtains limited information about the protein. Other nonoptical label-free imaging techniques such as low-dose cryo-electron microscopy (20) can be useful for studying static interaction states, but do not work as well with smaller proteins, and involve a trade-off between image contrast and radiation damage. Finally, circular dichroism (CD) spectroscopy (21) is a label-free nonimaging technique, which can provide limited information only about the secondary structures of protein. In Table 1, we compare our technique to these label-free molecular diagnostic tools (16–21). The list in Table 1 is not intended to be exhaustive or complete, but only sufficient to give an idea of how Raman fits into the existing suite of tools available to biologists and chemists. Examination of the table illustrates that TRIP excels at operation at near-physiological conditions as mentioned above. The high amount of overlap with other techniques establishes TRIP as a general advance-screening tool for a wide variety of protein–drug interactions. Also, its noninvasive nature allows the sample to afterward be examined with any of the methods.

In the following, the power of the TRIP method is first demonstrated by using a time-dependent binding; namely binding of 2,4 dinitrophenol (DNP) to transthyretin (TTR) protein. This protein is of relevance to important diseases, and its disease-causing action is to polymerize and form insoluble amyloid fibrils under certain conditions (22). DNP is one of the inhibitor drugs that can stop the fibrillation (polymerization) of TTR (22), therefore shedding light on their interaction is crucial for improving drug efficiency. Next, we used our technique to study more traditional binding interactions between streptavidin and biotin, considered one of the strongest bindings of protein and ligand, in order to compare to prior work and show advantages. Finally, we successfully demonstrated the technique for evaluating the bindings of 6 antigen–antibody systems, three involving protein A (SpA)-antibody (IgG) complexes and three involving severe acute respiratory syndrome (SARS) Cov 2 receptor–binding domain (RBD)-IgG complexes. These studies investigated the binding interactions of the eight protein–ligand pairs in their aqueous solution using Raman microscopy. Overall, the results of all experiments showed the applicability of TRIP to perform advanced screening of the bindings between proteins and ligands of all sizes. Furthermore, the TRIP technique saves time and money as it 1) requires no sample preparation, 2) uses less protein samples, 3) has fast detection time in minutes, 4) measures direct binding, and 5) uses low-cost extension on the existing system, thus demonstrating that this technique has the potential to do high-throughput screening of drugs (23).

Results

In general, the Raman spectral region between 500 cm^{-1} and 1,700 cm^{-1} is the richest with respect to information about proteins. It is called the fingerprint region, as it includes the vibrational modes of amino acids and their secondary structures. A full spectral assignment can be found in Table 2 (14, 24–27). The main

Table 1. Label-free protein-drug interaction-in-solution techniques

Techniques	Complex sample	Without surface attachment	Non-Invasive	Resolution of detection	Reproducibility	Data collection speed
Non-optical techniques						
X-ray/Neutron scattering (18)	Yes	Yes	No	Protein complex	moderate	hours
Cryo-electron microscopy (19)	No	Yes	No	Atomic	moderate	hours
Optical techniques						
Circular dichroism (20)	No	Yes	Yes	Protein backbone	high	minutes
Surface plasmon resonance (15)	No	No	No	Protein complex	high	minutes
Interferometry (16)	Yes	No	No	Protein complex	high	minutes
SERS (17)	Yes	No	No	Atomic	low	minutes
TRIP	Yes	Yes	Yes	Atomic	high	minutes

advantage of Raman spectroscopy is its faster spectral collection time compared to X-ray/neutron scattering and cryo-electron microscopy (19, 20), significantly with little to no sample preparation (water does not significantly interfere with the signal, as, for example, infrared spectroscopy). This makes it a strong candidate for real-time analysis (28). In order to use Raman microscopy to gain quantitative information about the relative amount of protein and ligand in a complex, one must know the Raman scattering intensities (cross sections) of both the protein and ligand. Here, Raman measurements were directly obtained from equimolar PBS solutions of the protein, ligand, and their mixes.

TRIP Detection of Time-Dependent Protein–Drug Binding. First, we studied the binding interactions of 2,4 dinitrophenol (DNP) to transthyretin (TTR). This study investigated time-dependent binding between TTR and DNP and the Raman microscopic study of the pair in their aqueous solutions. Because of their importance in medical field, their binding interactions were previously studied

Table 2. Raman band assignments of amino acids and secondary structures

Band cm	#	Vibrational mode assignment	Band cm[1]	#	Vibrational mode assignment
The amino acids					
Tryptophan (17)			Phenylalanine (18)		
757	1	Benzene stretch/pyrrole in-phase breathing	622	1	Ring deformation
877	2	N-H bending, indole ring vibration	1,002	2	Symmetric ring breathing, vibration
1,010	3	Pyrrole ring out-of-phase breathing	1,030	3	In-plane CH deformation
1,341	4	Fermi resonance between N-C in pyrrole ring	1,201	4	Phenyl C stretching
1,358	4	Fermi resonance between N-C in pyrrole ring	1,585	5	Ring stretch, doublet
1,555	5	C-C stretching, pyrrole ring	1,605	6	Ring stretch, doublet
Tyrosine (17, 18)			Other amino acids		
643	1	In-plane ring vibration	543/563		O=C–OH deform. - Threonine (18)
828	2	Tyrosine doublet/phenol ring breathing	744		C–OH twisting- Threonine (19)
858	2	Tyrosine doublet/phenol ring breathing	897		C–C–O stretching- Threonine (18)
1,175	3	CH2 twist and rock, CH-NH2	655		C–S stretching- Cysteine (18)
1,206	4	Phenyl C stretching	705		C–S stretching- Cysteine (18)
1,260	5	Ring stretch, benzene derivate	655		CH_2–S stretching- Methionine (18)
1,615	6	Ring stretch, benzene derivate	725		S–CH stretching- Methionine (18)
The secondary structures					
β-sheets (7, 17)			Alkyl C-N or Skeletal γC–C (7, 17)		
1,235 to 1,250	Amide III	N–H and C–H bend	1,050 to 1,170	C–N, γC–C	C–N or C–C stretch, NH_3
1,665 to 1,680	Amide I	H–bonded C=O stretch	Aliphatic side chain (7, 17)		
α-helices (7, 17)			890 to 920	ρCH_2	CH_2 deformation
930 to 950	Skeleton	N–C–C stretch	1,300 to 1,340	ρCH_2	CH deformation
1,270 to 1,300	Amide III	N–H and C–H bend	1,449 to 1,459	ρCH_2	CH and CH_3 deformations
1,650 to 1,655	Amide I	H–bonded C=O stretch	Disulfide bonds (20)		
Disordered (7, 17)			508 to 512	S-S	GGG conformers
1,250 to 1,270	Amide III	N–H and C–H bend	535 to 550	S-S	TGT conformers

(22) using a variety of techniques, with their dehydrated complexes investigated by Raman microscopy (29). Here, we investigated time-dependent binding interactions between TTR and DNP. Their binding interaction is studied by X-ray crystallography and it is illustrated in Fig. 2*A* (30). Fig. 2*B* shows the Raman spectra (their SEs shaded) taken from 20 μM TTR solution, 20 μM DNP solution, and 20 μM TTR+20 μM DNP solution at 0 to 1 h, 2 to 3 h, and 24 h (after the initial mixing). Note that the data are divided into three spectral ranges due to the spectrometer being automatically readjusted for each region by the commercial Raman spectrometer (Lab-Ram from Horiba). Note that the Raman spectra of DNP were nearly invisible compared to TTR (Fig. 2*B*), so that all the spectral changes in the mixes are due to the effects of binding. Comparing Raman spectra of TTR and the mixes, clearly shows significant spectral changes in the spectral regions of 800 to 930 cm^{-1} and 1,230 to 1,350 cm^{-1}, which are evidence of binding-induced interactions between the DNP and the TTR. PCA of the Raman data for both regions are shown in Fig. 2*C*. Considering the Raman data obtained from three different days, the PCA clustering of the repeats from the same sample, meaning the data were highly reproducible. Both PC-1 components separated DNP from other samples very well (Fig. 2*C*).

In the first spectral region, the clusters of the TTR and the DNP+TTR mixes were clearly separated by PC 2 component, but the clusters of the mixes for 0 to 1 h, 2 to 3 h, and 24 h overlapped (Fig. 2*C*). In this region, the bound DNP samples were mostly in the positive side (positive side from separating line at zero) of PC 2, meaning that the positive peaks (red numbered) of the PC 2

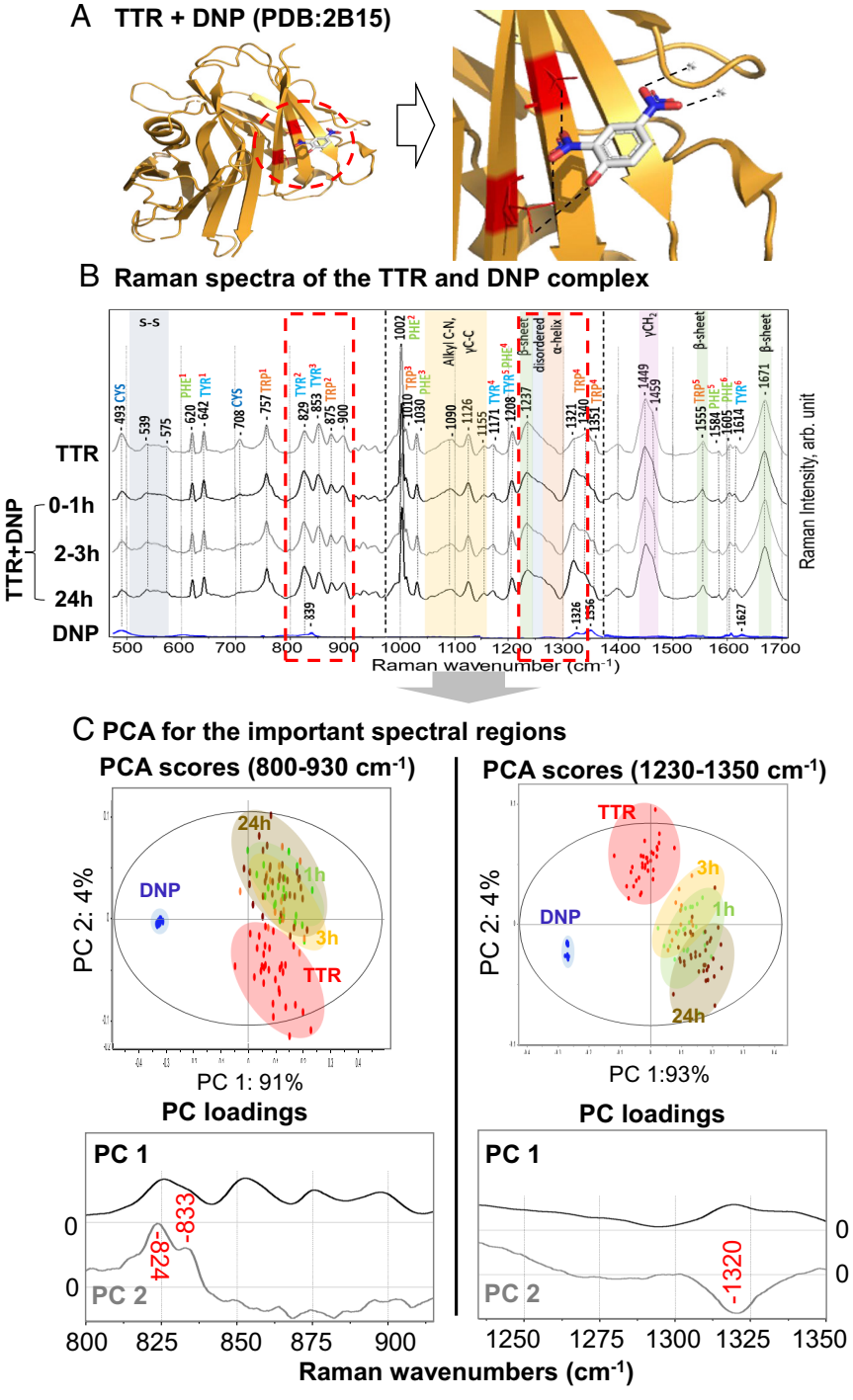

Fig. 2. (*A*) Molecular structure of the TTR (orange) – DNP (white: nitrogen molecule-blue, oxygen molecule - red) complex (PDB:2B15) with interacting Serine 117 and Alanine 108 of TTR marked in red: two hydrogen bonds (marked black stripe lines) between one of the DNP's nitro groups (NO_2) with serine 117 and alanine 108, two hydrogen bonds between other DNP's nitro group and two water molecules, and one hydrogen bond between DNP's OH of the phenolic ring and serine 117, (*B*) Raman spectra of TTR, TTR-DNP mixes, and DNP (blue) with their SEs (shaded: n_{each}= 38–43) (*C*) PCA score plots and loadings of the 800 to 930 cm^{-1} and the 1,230 to 1,350 cm^{-1} regions (In the score plots: each dot represents one spectrum. In the loadings: the red numbered Raman bands were changed due to the binding).

loading are changed the most for the bound protein samples. Especially, the bound DNP's phenolic ring's OH stretching mode at 824 cm^{-1} enhanced due to forming a hydrogen bond with TTR's Serine 117 (Fig. 2*A*). The second highest peak of the PC 2 loading was at 833 cm^{-1}. DNP's in-plane bending mode of the two NO_2 (nitro) groups at 839 cm^{-1} shifted to 833 cm^{-1} and enhanced when these nitro groups formed hydrogen bonds with TTR's serine 117, alanine 108 and two free water molecules (Fig. 2*A*).

Most interestingly, the PC 2 component of the second spectral region (Fig. 2*C*), separates not only the unbound protein cluster from the bound protein clusters but also the 24-h-bound cluster from other bound clusters. That means the binding between DNP and the protein was enhanced over time. In particular the 1,320 cm^{-1} line was most heavily weighted in PC 2, where the bound DNP samples became more negative meaning that the strength of the binding increased in 24 h. The line is implicated in the DNP's stretching mode between the aromatic ring and two NO_2 (nitro group) at 1,320 to 1,330 cm^{-1} (31). It has a Raman shift of 1,320 cm^{-1} in the bound DNP solutions (Fig. 2*C*), which is clearly shifted relative to the corresponding spectra of the unbound DNP solution at 1,326 cm^{-1} (Fig. 2*B*). This low-frequency shift is possibly due to hydrogen bonds that are expected to form between DNP's two nitro groups and TTR's serine 117, alanine 108, two free water molecules (Fig. 2*A*) and its intensity enhanced from 0 to 24 h after their binding.

Conclusion is that DNP's two nitro groups' stretching mode from the aromatic ring changed over 24 h but their in-plane bending mode did not change after initial binding. These results, especially in the last spectral region, demonstrate the TRIP technique's capability to successfully detect the time-dependent binding interactions between the TTR and DNP solutions.

TRIP Detection of Static Protein–Drug Binding. Next, we studied the streptavidin–biotin complex. This complex was chosen because it is a strong interaction and well-studied in the literature. Therefore, it provides a good opportunity to demonstrate the power of the TRIP technique. This study investigated the binding interactions between streptavidin and biotin in their aqueous solutions using Raman microscopy. Their binding interaction in their anhydrous forms was studied previously using the difference-Raman techniques (12). The strong noncovalent binding of biotin (vitamin H) to streptavidin derives from multiple types of interaction between the streptavidin and biotin (32), as illustrated in Fig. 3*A*. Biotin's Raman spectra are nearly invisible compared to streptavidin (Fig. 3*B*), so all the spectral changes in their mixes are due to their binding. We applied PCA for all three spectral regions, and their results are shown in Fig. 3*C*. In all regions, the PC-1 components separated biotin from bound and unbound streptavidin samples as we expected. To separate the bound from unreacted streptavidin spectra, it is seen that the PC-2, with assistance from PC-1, works best in region I of the spectra. In this region, the negative peaks (red numbers in Fig. 3*B*) of the PC 2 loading are changed most when biotin bound with streptavidin. The strongest negative peak in this loading was the tryptophan (TRP) band at 870 cm^{-1} due to the N-H bending of the indole ring. This band shifted from 877 cm^{-1} to 870 cm^{-1} for unbound versus bound streptavidin solutions. This band (33) is sensitive to the hydrogen bonding that is implicated in protein–ligand binding. Due to the protein–ligand binding, both the frequency shift and strength of the band changed, indicating that strong hydrogen bonding occurred at the N-H group. This means at least one tryptophan molecule of the streptavidin is involved in hydrogen bonding with the biotin, consistent with X-ray crystallography data (34) indicating the presence of four tryptophan (TRP-79, 92,108, and 120) residues in the biotin-binding site of streptavidin (Fig. 3*A*). The next strongest negative peaks of the PC-2 loadings were the tyrosine's Fermi doublet at 845 cm^{-1} and 818 cm^{-1} that were shifted from 853 and 830, respectively, for the bound streptavidin solutions. This doublet's intensity ratio (I_{850}/I_{828}) is sensitive to the hydrogen bonding of the phenolic OH group of tyrosine (35). The same X ray study (34) showed that one tyrosine (TYR-43) formed a hydrogen bond with the biotin (Fig. 3*A*). The next binding-relevant peak was a broad spectral area centered at 910 cm^{-1}, which correspond to CH_2 deformation (ρCH_2), and its intensity increased for the bound streptavidin samples. In region II, positive PC-3 component alone separates the bound and unbound spectra, and this component explained only 1% of the variance of the data. The positive peaks of the PC-3 loading correspond to the secondary structures such as disordered at 1,260 cm^{-1} and alpha-helix at 1,275 cm^{-1}. These secondary structure changes could happen due to an interaction between biotin and the alpha helix of the streptavidin (34). In region III, the separation is poor for all PCA components. In contrast to the prior difference-Raman study of this interaction (36), the samples do not have to be dried, and the our results proved statistically reliable measurements by the TRIP.

TRIP Detection of Antigen-Antibody Binding. Monoclonal antibodies offer a major advantage in drug discovery, and it became easy to quickly make a lot of new antibodies. However, the process of assessing antibodies to find promising drug candidates is time-consuming and expensive, and all prospects fail to be considered. Here, we offer a drug-screening technique that is time-saving and cost-effective. To show the ability of TRIP to work with more complex molecules, we studied the binding interactions between protein A (SpA) and three antibodies (two monoclonals and one polyclonal). This study investigated the binding interactions between SpA and monoclonal/polyclonal antibodies in their aqueous solution using Raman microscopy. Fig. 4 examines the interactions of antibodies with SpA. Again, this interaction is chosen because it is well-studied by other techniques (37) and their drop dried complex previously studied by Raman (11). Fig. 4*A* lists the experimental samples of the study. Fig. 4*B* shows the measured Raman spectra from the experimental samples. One can see the significant spectral changes between the Raman spectra of unbound and bound antibodies for all three antibody complexes in Fig. 4*B*. This means SpA bonded with all three antibodies. The PCA of Raman data for these complexes are in Fig. 4*C*. The PC-1 components are separating the bound antibody samples from unbound antibodies in all spectral regions, and the relevant peaks are red numbered in the PC-1 loadings. All samples were separated into clusters with minimal overlap, except for goat and human antibodies. Nonetheless, they are partially separated in regions II and III. Interestingly, these two antibodies are cleanly separated when the SpA is mixed in, especially in the main "fingerprint" region I. Here, it should be noted that the goat antibodies are polyclonal whereas the human and mouse are monoclonal. The strongest relevant Raman peaks for the bound antibodies were the α-helix's CH_3 groups at 938, the amide III region at 1,320 to 1,340, and the amide I region at 1,655 cm^{-1} bands, which were observed in the SpA spectra (Fig. 4*B*). This means α-helices increased in all bound antibodies due to their bonding with the alpha helical SpA. Also, the band at 900 cm^{-1} assigned to the CH_2 deformation was increased in the bound antibodies. We observed a similar increase for the ρCH_2 band in the bound streptavidin sample (Fig. 3*C*). The next important peaks for the bound antibodies were phenylalanine's 620, 1,003, and 1,605 cm^{-1} bands. Their intensities were increased in all

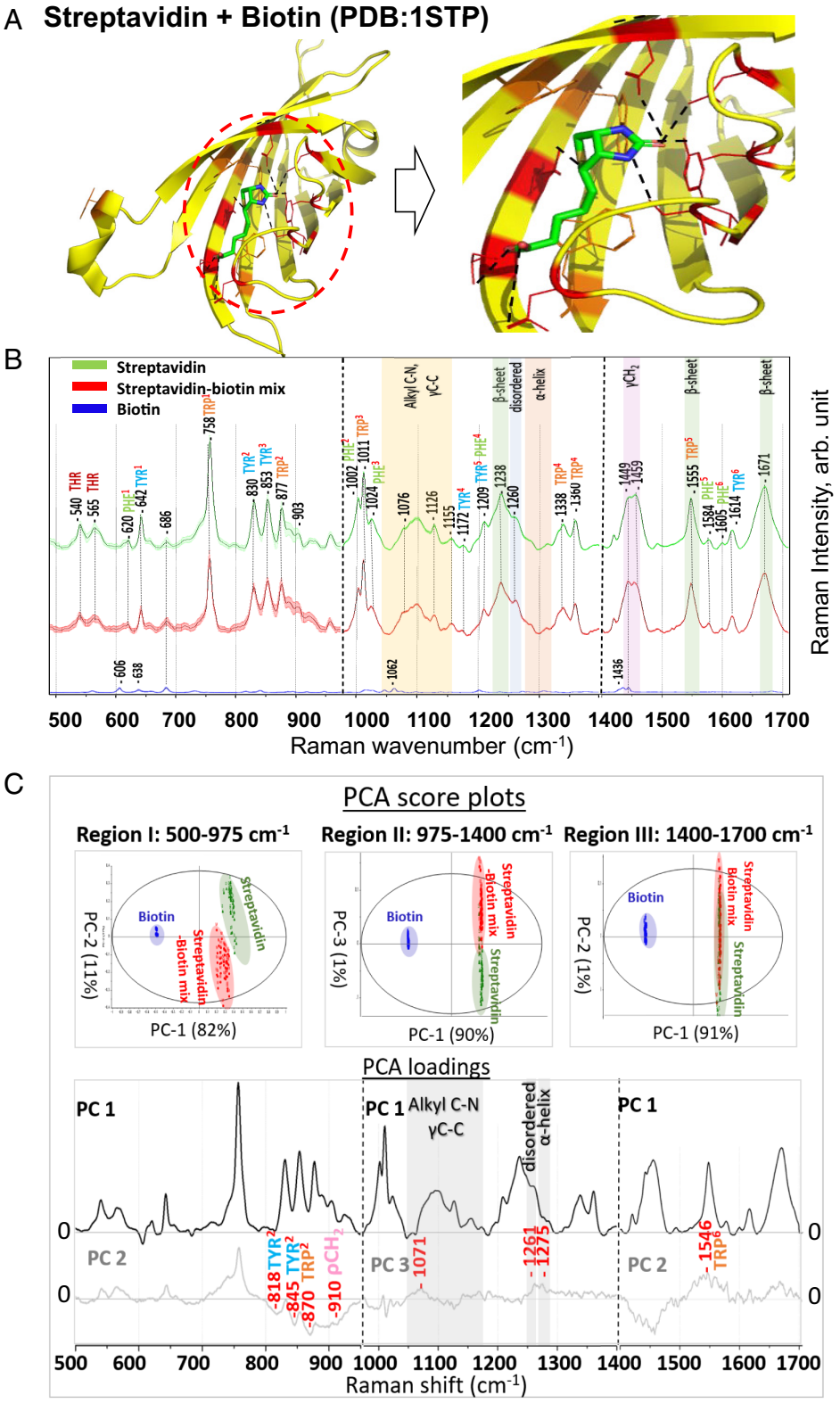

Fig. 3. (*A*) Molecular structure of the streptavidin (yellow) – biotin (green: nitrogen molecule-blue, oxygen molecule-red, sulfur molecule-yellow, double bond-light red) complex (PDB:1STP): biotin hydrogen bonded with streptavidin's serine 27, 45, 88, asparagine 23, aspartic acid 128, and tyrosine 43 in red; interacting residues of streptavidin's Tryptophan 79, 92, 108, and 120 in orange, (*B*) Raman spectra of streptavidin (green), streptavidin-biotin mix (red), and biotin (blue) with their SEs (shaded: n_{each}= 35–40), (*C*) PCA score plots and loadings of the first, second, and third principal components of all measured Raman spectra are shown (In the score plots: each dot represents one spectrum. In the loadings: the red numbered Raman bands were changed due to the binding).

bound antibodies. Phenylalanine's 1,003 peak is sensitive to the hydrophobicity of the local environment (38). This means the binding between SpA and IgG could be partially driven by hydrophobicity. The region from 705 to 744 cm^{-1} corresponds to C-S stretching of cysteine, threonine's C-OO wagging, and C-OH stretching. The intensities of these bands were increased in the bound antibodies. Also, the intensities of the other two threonine bands at 561 and 573 cm^{-1} corresponding to C–C stretching and C–OOH stretching of threonine increased. The last relevant peak was at 1,183 cm^{-1}, which corresponds to CH_2 twist and rock of multiple amino acids.

Last, our technique was applied to an unknown interaction; namely the interactions of SARS Cov 2 spike protein RBD with the three antibodies that were used in the previous experiment with SpA. This study examined the binding interactions between SARS Cov 2 RBD and antibodies in their aqueous solution using

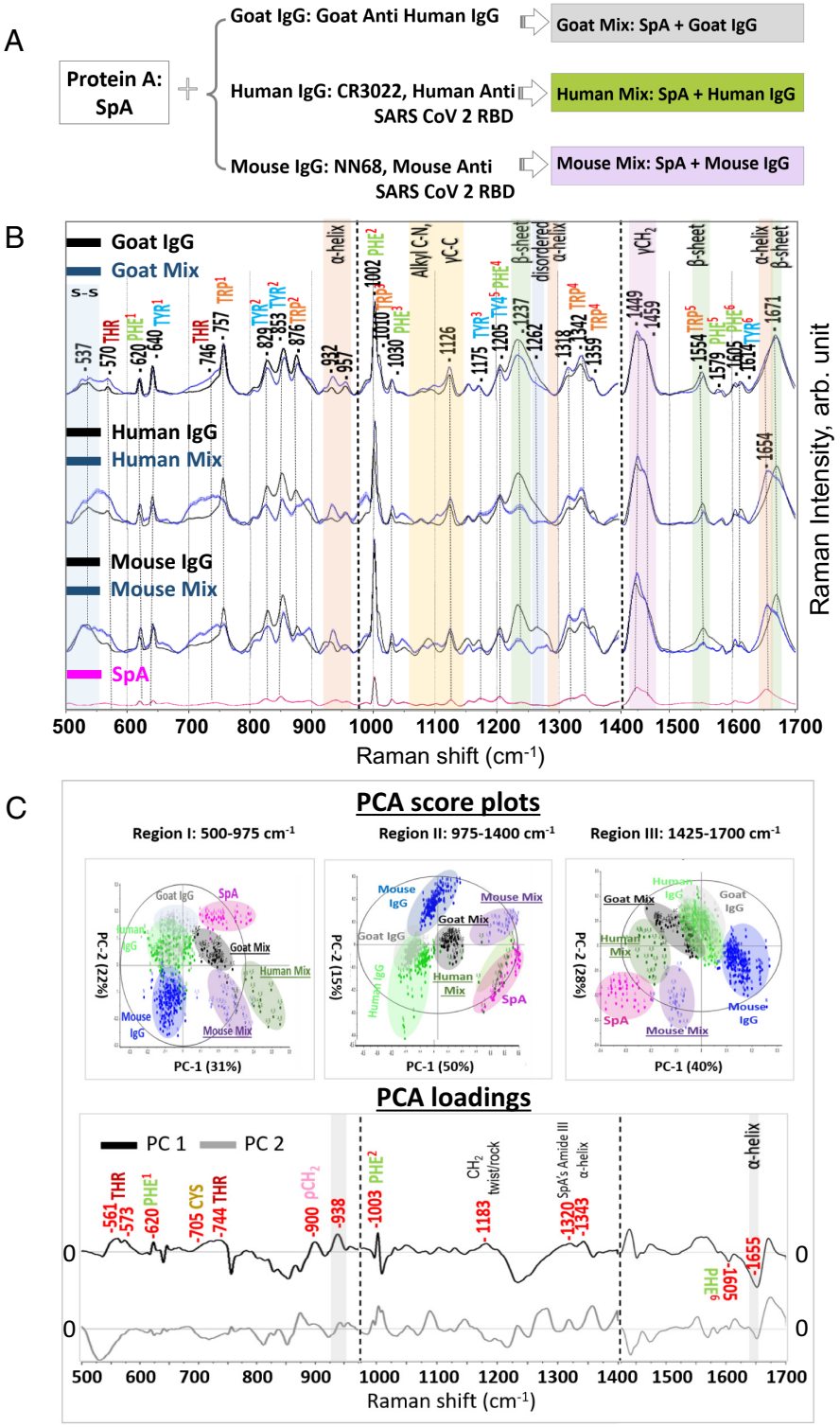

Fig. 4. (*A*) The protein samples of the SpA and antibody complexes, (*B*) Raman spectra of antibodies (black), their SpA mixes (blue) and SpA (pink) with their SEs (shaded), (*C*) PCA score plots and loadings of the first two principal components are shown (In the score plots: each dot represents one spectrum. In the loadings: the red numbered Raman bands were changed due to the binding).

Raman microscopy. These two antigens bind with different parts of antibodies. SpA binds with the FC region of antibodies, while RBD binds with their Fab region. The goat IgG did not bind with RBD, whereas the human IgG and mouse IgG did bind with it. Also, the mouse IgG neutralized RBD by binding its ACE 2 region. For simplification, we named the mix of RBD and goat IgG as nonbinding mix, the mix of RBD and Human IgG as binding mix, and the mix of RBD and mouse IgG as neutralizing mix. Of note, the RBD-binding sites to human IgG (39) and the ACE 2-binding sites (40) of a neutralizing IgG were previously studied by X-ray crystallography. The RBD and antibody experimental samples are listed in Fig. 5*A*. Raman spectra taken from the experimental samples are shown in Fig. 5*B*. Examination of Raman spectra in Fig. 5*B* shows a small difference in the spectrum for the goat antibody, but larger differences for the other two antibodies, which are similar in most spectral regions yet are clearly not identical. Note here that the intensities of the spectral changes for the RBD-bound antibody samples (Fig. 5*B*) were much smaller than the intensities of the spectral changes in the SpA-bound antibody samples (Fig. 4*B*). Fig. 5*C* shows the PCAs of Raman

data where the PC-2, 3 & 4 components give the best separation in a particular spectral region. Here, it is seen that in all cases the PCA cannot distinguish well between the cluster of the goat antibodies (gray) and the cluster of the nonbinding mix (black) in Fig. 5*C*. This is as expected since the goat antibodies are considered noninteracting and therefore should not bind. In contrast, the human and the mouse antibodies are well separated after mixing with Cov 2 RBD. The relevant peaks separating the bound antibodies from the unbound antibodies are numbered and colored in red in Fig. 5*C*. As seen with the SpA-bound antibody samples, phenylalanine's 623, 1,000, 1,028, and 1,605 cm^{-1} bands, threonine bands at 556 and 572 cm^{-1}, and the spectral region between 705 cm^{-1} and 738 cm^{-1} are increased for the RBD-bound antibody samples. The spectral changes that differed between the RBD-bound antibodies and the SpA-bound antibodies were the intensity increases in tyrosine's parasubstituted

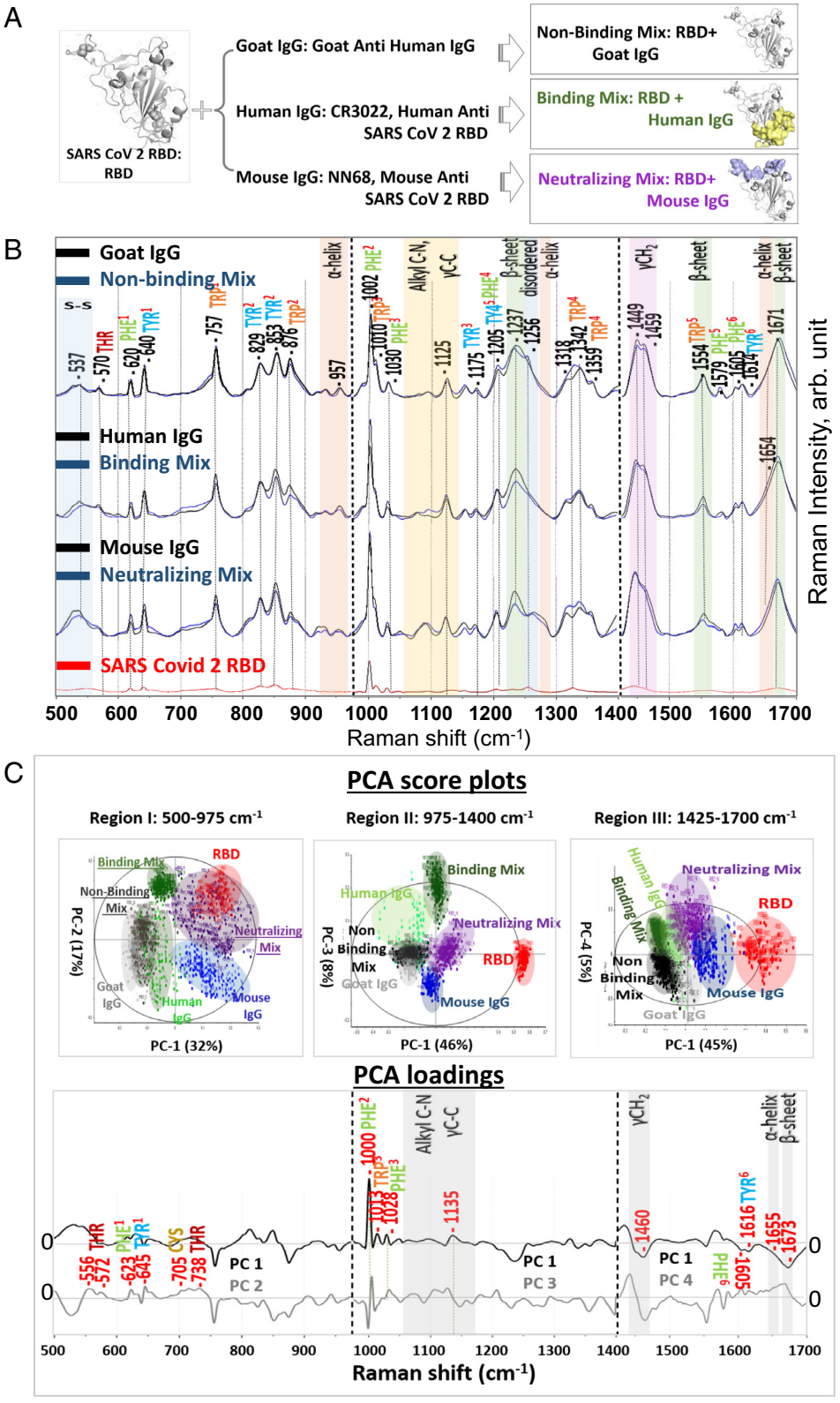

Fig. 5. (*A*) Illustration of binding sites of RBD and the human IgG (yellow) and RBD and the mouse IgG (blue): PDB,6SF, note: the binding sites do not overlap. (*B*) Raman spectra of antibodies (black), their RBD mixes (blue) and RBD (red) with their SEs (shaded), (*C*) PCA score plots and loadings of the first, second/third/fourth principal components of all measured Raman spectra are shown (In the score plots: each dot represents one spectrum. In the loadings: the red numbered Raman bands were changed due to the binding).

benzene ring at 645 cm^1 and tyrosine's ring stretch at 1,616 cm^{-1}. These tyrosine vibrational modes were previously studied for the hydrogen bonding of tyrosine (41). Also, the changes in the tryptophan's ring breathing at 1,013 cm^{-1} happened in the bound samples, and this band is sensitive to the cation–pi interaction (42). The binding interaction between the human IgG and RBD was studied via X-ray crystallography (39), and it showed that 2 tryptophan and 4 tyrosine molecules are involved with direct binding between them. The numerous Raman peaks in the relevant PC loadings correspond to secondary structures such as alkyl C-N or backbone skeletal γC-C bands at 1,083 cm^{-1}, aliphatic side chain at 1,460 cm^{-1}, the β-sheets at 1,673 cm^{-1}, and α-helices at 1,655 cm^{-1} for the RBD-bound antibodies.

Discussion

We have developed a thermostable Raman interaction profiling (TRIP) technique for a label-free drug screening for a broad range of ligands, from small drugs to large antibodies, in their PBS solutions. TRIP is both efficient and cost-effective due to its fast detection time, lack of a need for sample preparation or a large protein sample, direct binding measurement, and low-cost extension on an existing system. We successfully applied our technique to two protein–drug and six antigen–antibody complexes. Furthermore, we demonstrated its capability in detecting the time-dependent binding interactions between the TTR and DNP.

Our TRIP technique has advantage in requiring no surface attachment and no sample preparation over the existing label-free protein–drug interaction techniques such as SPR, interferometry, and SERS. In comparison with other existing techniques such as X-ray/neutron scattering, cryo-electron microscopy, and CD, TRIP technique has advantages in having higher (single amino acid) detection resolution than X-ray/neutron scattering, CD, and having higher speed and higher reproducibility than cryo-electron microscopy and X-ray/neutron scattering. It is noninvasive, therefore its samples could be interrogated by multiple techniques.

Further extensions of TRIP could include development of high-throughput drug screening (perhaps using multiwell plates each containing mix of the same target protein and various drugs) as well as applications to study side effects of drug via real-time detection of interactions between the drug and target protein. Also, it could be used in scanning protein pools for virus–host interactions and cytoplasmic extracts for interactions between a new drug and the entire cellular proteome. In addition, its broad applicability not only for small drugs but also for antibodies allows it to be developed as a universal protein–ligand interaction profiling tool for the structural molecular science and pharmaceutical industry. For example, our goat antibody (Goat Anti-Human) is a complex protein mixture already (versus single antibody).

Materials and Methods

Sample Preparation. SpA (Cat. No. p6031), TTR (Cat. No. P1742), DNP (Cat. No. D198501), and biotin (Cat. No. B4501) were purchased from Sigma Aldrich. The receptor-binding domain (RBD) (residues 319 to 541) of the SARS CoV-2 spike (S) protein (GenBank: QHD43416) was purchased from BEI resources, Human Anti-SARS CoV S IgG1 (CR3022) was purchased from the Absolute Antibody, and Mouse Anti-SARS CoV-2 Spike Neutralizing IgG2b (clone NN68) was purchased from the Creative Diagnostics. Streptavidin (Cat. No. 21135) and Goat Anti-Human IgG (GAH) (Cat. No. 62-8400) were purchased from the Thermo Fisher Scientific. The RBD and three antibodies were used as received without purification. Sterilized 0.01 M PBS of pH 7.4 was used as protein and drug solvent. PBS was used to prepare TTR (20 μM), DNP (20 μM), streptavidin (3 mg/mL), biotin (0.055 mg/mL), and SpA (3 mg/mL) solutions. TTR and DNP solutions were mixed in a 1:1 molar ratio and stored at 4 °C. Raman measurements performed 10 μL samples from the mix at 0 to 1 h, 2 to 3 h, and 24 h after their mixing. Streptavidin and biotin solution was mixed in a 1:4 (due to tetrameric structure of streptavidin) molar ratio and incubated overnight at 4 °C. This mix's final concentration was 1.53 mg/mL. The original RBD and three antibody solutions were 1 mg/mL in 0.01 M PBS buffer. We concentrated these solutions three times using the Amicon Ultra-0.5 centrifugal filter (Cat. no. UFC500308), and their final concentrations were 3 mg/mL. Each antigen (RBD or SpA) and antibody (CR3022 or NN68 or GAH) were mixed in a molar ratio of 1:1 and incubated overnight at 4 °C. The final concentrations of the RBD +IgG mixes were 1.75 mg/mL, and the SpA +IgG mixes' concentrations were 1.875 mg/mL.

Apparatus and Software. The protein samples were studied using the LabRam Raman confocal system from Horiba. The overall microscope setup is shown in Fig. 6*A*. The excitation laser was 785 nm. Raman measurements were taken from a 10 μL drop of solution deposited on Au-coated glass slide (Ted Pella No 26002-G). The cooled Au thin layer on a glass slide served double purposes for dissipating thermal energy from the excitation laser and for blocking the fluorescent background from the glass substrate. The laser is focused to a one-micron spot size inside the liquid samples using a 100X microscope objective lens with 0.75 NA. The acquisition time was 5 s and averaged by 12 spectra. The laser power was 7 mW. A key part of this study was to minimize sample damage by the laser excitation. Spontaneous Raman generation is not an efficient process. Therefore, for the small quantities of material used in Raman microscopy, relatively high laser intensities are often needed to see a high-quality Raman spectrum. Even though we excite the sample at infrared wavelength 785 nm, which is well inside the biological transparency window, significant laser heating was seen. In particular, for a sample at room temperature, the Raman spectra changed with time, especially for the RBD protein sample, which we attributed to denaturation. To address the sample heating problem, we developed a simple, compact cooler driven by a thermoelectric device. The cooler was able to rapidly cool to near ~10 °C in about 10 s. To avoid water condensation, the sample was hermetically sealed using a window consisting of a microscope coverslip bonded to a clamp device that could be quickly opened and closed. Due to the low clearance of the microscope stage, it was necessary to make the cooler highly compact. The final version of the cooler is shown in Fig. 6*A*. On the bottom is a small fan and heat sink. The coverslip, giving optical access to the sample, is sealed with a gasket-glue. Another gasket is placed between the two metal plates. Since the glass slide has poor thermal conductivity, a thermal two-sided tape was used to contact between the cool side of the TEC and the slide. In addition, to investigate possible interference by the gold layer, we performed dry-state measurements of our samples by allowing the drop to dry in air onto the gold layer. We observed some inconsistencies in Raman spectra due to random orientation of dried protein samples rather than interference by the gold layer.

The backgrounds of the Raman raw spectra were estimated by the "EstimatedBackground" function of the Mathematica 12.1 (Wolframs). It is based on a statistics-sensitive nonlinear iterative peak-clipping algorithm that estimates background while trying to preserve features of the spectra (43). After the estimated backgrounds removed from the raw spectra, the background-removed spectra were normalized by unit-vector (vector norm) using the OriginPro software. Furthermore, the normalized spectra were smoothed with the Savitsky-Golay algorithm with 15 adjacent points by the OriginPro software. Fig. 6*B* shows the preprocessing steps of the Raman spectrum from the mouse IgG sample. The processed Raman spectra from three different samplings are depicted in Fig. 6*C*.

PCA Analysis. Raman spectra of the mixtures of protein–ligand and protein–protein are very complex. Therefore, a univariate presentation of their Raman spectra is not feasible, and a multivariate method has been chosen using PCA. PCA is a statistical method that increases interpretability in a dataset while minimizing loss of information, allowing us to understand the factors that affect spectral variation in the data as will be shown below (44, 45). Our data matrix is created where the rows contain sample information and the columns (variables) are Raman intensities on corresponding wavenumber. PCA aligns a set of axes, called principal components (PCs), with the maximal directions of variance within a dataset using the covariance matrix of the original data. PCA then results in three matrices that contain the scores, the loadings, and the residuals. The score matrix indicates the difference among groups of samples, and the loading plot corresponds to the variance in the

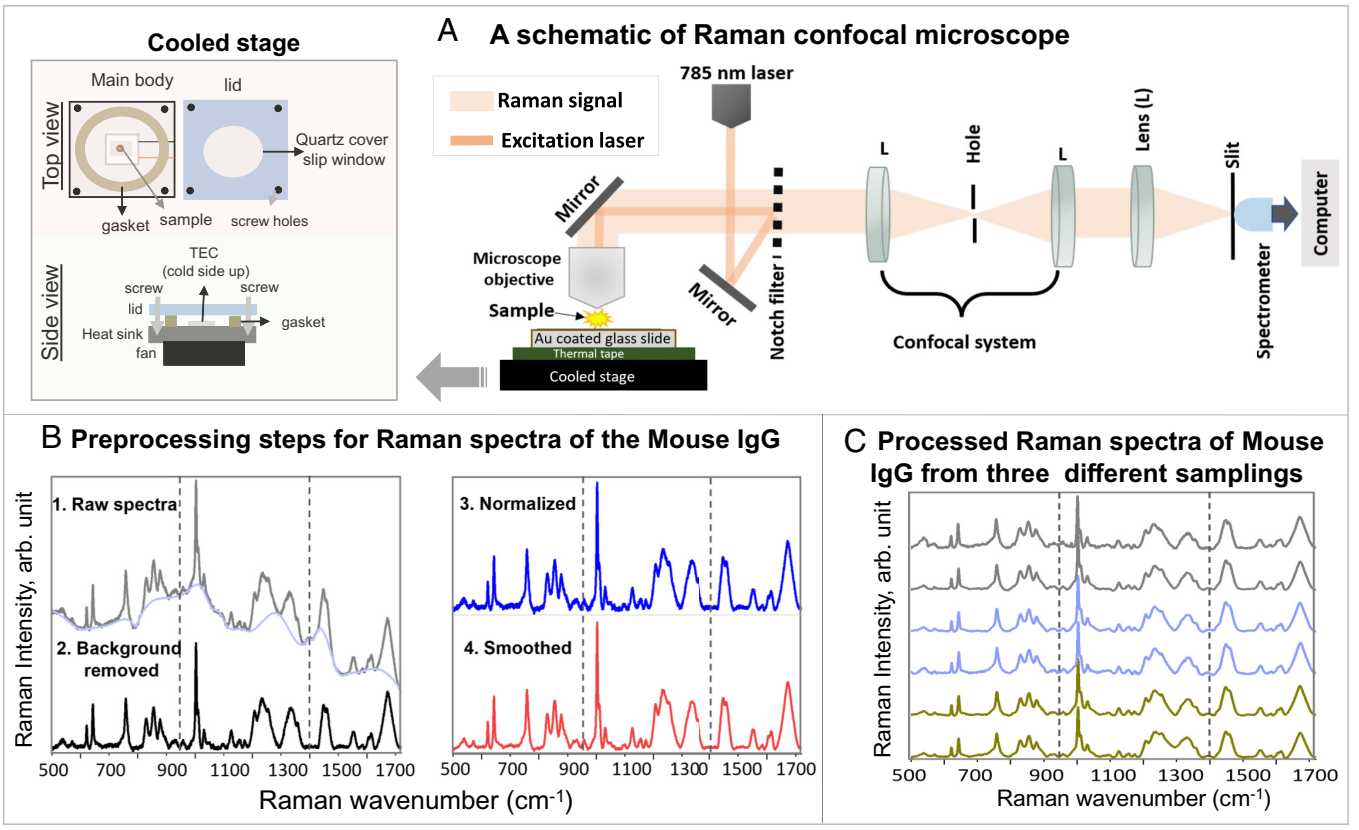

Fig. 6. (*A*) A schematic of Raman confocal microscope and a sketch of thermoelectric cooling device used to cool the protein solution samples on the microscope stage, (*B*) Preprocessing steps for Raman spectra of the Mouse IgG, (*C*) Processed Raman spectra of the mouse IgG from three different samplings (sampling 1-gray, sampling 2-light blue, and sampling 3-light green).

Raman spectra. The use of PCA thus allows us to better interpret complex Raman spectra of different antigen and antibody mixes by showing differences between the samples and connecting them to differences in the variables defining a sample. Past work has shown the successful application of PCA to interpret spectral variation (45). The PCA was performed by Aspen Unscrambler software.

Data, Materials, and Software Availability. All study data are included in the main text.

ACKNOWLEDGMENTS. We acknowledge the support of Air Force Office of Scientific Research Award No. FA9550-20-1-0366, Office of Naval Research Award No. N00014-20-1-2184, Robert A. Welch Foundation Grant No. A-1261 and A-1547. P.R.H. is supported by the Army Research Laboratory Cooperative Agreement W911NF-16-2-0094. B.W.N. is supported by Texas A&M University X Grants Program, Round 4. V.V.Y. is supported by the NIH Grant No. 1R01GM127696, 1R21GM142107, and 1R21CA269099.

Author affiliations: [a]Institute of Quantum Science and Engineering, Texas A&M University, College Station, TX 77843; [b]Physics Department, Baylor University, Waco, TX 76798; and [c]Airspace Engineering Department, Princeton University, Princeton, NJ 08544

1. K. S. Lam *et al.*, A new type of synthetic peptide library for identifying ligand-binding activity. *Nature* **354**, 82–84 (1991).
2. D. E. Gordon *et al.*, A SARS-CoV-2 protein interaction map reveals targets for drug repurposing. *Nature* **583**, 459–468 (2020).
3. M. J. Keiser *et al.*, Predicting new molecular targets for known drugs. *Nature* **462**, 175–181 (2009).
4. J. Zhang, R. E. Campbell, A. Y. Ting, R. Y. Tsien, Creating new fluorescent probes for cell biology. *Nat. Rev. Mol. Cell Biol.* **3**, 906–918 (2002).
5. A. J. Enright, I. Iliopoulos, N. C. Kyrpides, C. A. Ouzounis, Protein interaction maps for complete genomes based on gene fusion events. *Nature* **402**, 86–90 (1999).
6. D. Yang *et al.*, G protein-coupled receptors: Structure- and function-based drug discovery. *Signal Transduct Target Ther.* **6**, 1–27 (2021).
7. C. S. Adamson *et al.*, Antiviral drug discovery: Preparing for the next pandemic. *Chem. Soc. Rev.* **50**, 3647–3655 (2021).
8. Q. Liu, H.-G. Wang, Anti-cancer drug discovery and development. *Commun. Integr. Biol.* **5**, 557–565 (2012).
9. J. Hughes, S. Rees, S. Kalindjian, K. Philpott, Principles of early drug discovery. *Br. J. Pharmacol.* **162**, 1239–1249 (2011).
10. S. A. Oladepo *et al.*, UV resonance Raman investigations of peptide and protein structure and dynamics. *Chem. Rev.* **112**, 2604–2628 (2012).
11. R. P. Kengne-Momo *et al.*, Protein interactions investigated by the Raman spectroscopy for biosensor applications. *Int. J. Spectr.* **2012**, e462901 (2012).
12. A. Torreggiani, G. Fini, The binding of biotin analogues by streptavidin: A Raman spectroscopic study. *Biospectroscopy* **4**, 197–208 (1998).
13. A. Toyama, A. Matsubuchi, N. Fujimoto, H. Takeuchi, Isotope-edited UV Raman spectroscopy of protein–DNA interactions: Binding modes of cyclic AMP receptor protein to a natural DNA recognition site. *J. Raman Spectr.* **36**, 300–306 (2005).
14. R. W. Williams, "Protein secondary structure analysis using Raman amide I and amide III spectra" in *Methods in Enzymology* (Elsevier, 1986), **vol. 130**, pp. 311–331, https://linkinghub.elsevier.com/retrieve/pii/0076687986300168.
15. T. Miura, G. J. Thomas, "Raman spectroscopy of proteins and their assemblies" in *Proteins: Structure, Function, and Engineering*, B. B. Biswas, S. Roy, Eds. (Springer, US, Boston, MA, 1995), pp. 55–99, 10.1007/978-1-4899-1727-0_3.
16. H. H. Nguyen, J. Park, S. Kang, M. Kim, Surface plasmon resonance: A versatile technique for biosensor applications. *Sensors (Basel).* **15**, 10481–10510 (2015).
17. N. B. Shah, T. M. Duncan, Bio-layer interferometry for measuring kinetics of protein-protein interactions and allosteric ligand effects. *J. Vis. Exp.* e51383 (2014).
18. S. K. Gahlaut *et al.*, SERS platform for dengue diagnosis from clinical samples employing a hand held Raman spectrometer. *Anal. Chem.* **92**, 2527–2534 (2020).
19. L. A. Feigin, D. I. Svergun, *Structure Analysis by Small-Angle X-Ray and Neutron Scattering,* G. W. Taylor, Ed. (Springer, New York, NY, 1987), (https://link.springer.com/book/10.1007/978-1-4757-6624-0).
20. J. L. S. Milne *et al.*, Cryo-electron microscopy – a primer for the non-microscopist. *FEBS J.* **280**, 28–45 (2013).
21. N. J. Greenfield, Methods to estimate the conformation of proteins and polypeptides from circular dichroism data. *Anal. Biochem.* **235**, 1–10 (1996).
22. P. Raghu, G. B. Reddy, B. Sivakumar, Inhibition of transthyretin amyloid fibril formation by 2,4-Dinitrophenol through tetramer stabilization. *Arch. Biochem. Biophys.* **400**, 43–47 (2002).
23. I. W. Schie *et al.*, High-throughput screening Raman spectroscopy platform for label-free cellomics. *Anal. Chem.* **90**, 2023–2030 (2018).
24. T. Kitagawa, S. Hirota, "Raman Spectroscopy of Proteins" in *Handbook of Vibrational Spectroscopy*, P. Griffiths, J. M. Chalmers, Eds. (John Wiley & Sons Ltd, 2006).

25. D. Lin-Vien, N. Colthup, W. Fateley, J. Grasselli, *The Handbook of Infrared and Raman Characteristic Frequencies of Organic Molecules* (Elsevier, ed. 1, 1991), https://www.elsevier.com/books/the-handbook-of-infrared-and-raman-characteristic-frequencies-of-organic-molecules/lin-vien/978-0-08-057116-4.
26. B. L. Silva *et al.*, Polarized Raman spectra and infrared analysis of vibrational modes in l-Threonine crystals. *Braz. J. Phys.* **28**, 19–24 (1998).
27. H. Sugeta, A. Go, T. Miyazawa, Vibrational spectra and molecular conformations of dialkyl disulfides. *Bull. Chem. Soc. Japan* **46**, 3707–3411 (1973), 10.1246/BCSJ.46.3407.
28. H. Lui, J. Zhao, D. McLean, H. Zeng, Real-time Raman spectroscopy for in vivo skin cancer diagnosis. *Cancer Res.* **72**, 2491–2500 (2012).
29. Y. Xie, D. Zhang, D. Ben-Amotz, Protein–ligand binding detected using ultrafiltration Raman difference spectroscopy. *Anal. Biochem.* **373**, 154–160 (2008).
30. E. Morais-de-Sá, R. M. Neto-Silva, P. J. B. Pereira, M. J. Saraiva, A. M. Damas, The binding of 2,4-dinitrophenol to wild-type and amyloidogenic transthyretin. *Acta Cryst D.* **62**, 512–519 (2006).
31. V. Chiş, Molecular and vibrational structure of 2,4-dinitrophenol: FT-IR, FT-Raman and quantum chemical calculations. *Chem. Phys.* **300**, 1–11 (2004).
32. P. C. Weber, D. H. Ohlendorf, J. J. Wendoloski, F. R. Salemme, Structural origins of high-affinity biotin binding to streptavidin. *Science* **243**, 85–88 (1989), 10.1126/science.2911722.
33. T. Miura, H. Takeuchi, I. Harada, Characterization of individual tryptophan side chains in proteins using Raman spectroscopy and hydrogen-deuterium exchange kinetics. *Biochemistry* **27**, 88–94 (1988).
34. P. C. Weber, D. H. Ohlendorf, J. J. Wendoloski, F. R. Salemme, Structural origins of high-affinity biotin binding to streptavidin. *Science* **243**, 85–88 (1989).
35. M. N. Siamwiza *et al.*, Interpretation of the doublet at 850 and 830 cm^{-1} in the Raman spectra of tyrosyl residues in proteins and certain model compounds. *Biochemistry* **14**, 4870–4876 (1975).
36. A. Torreggiani, G. Fini, The binding of biotin analogues by streptavidin: A Raman spectroscopic study. *Biospectroscopy* **4**, 197–208 (1998).
37. A. R. Cruz *et al.*, Staphylococcal protein A inhibits complement activation by interfering with IgG hexamer formation. *Proc. Natl. Acad. Sci. U.S.A.* **118**, e2016772118 (2021).
38. Z.-Q. Wen, Raman spectroscopy of protein pharmaceuticals. *J. Pharm. Sci.* **96**, 2861–2878 (2007).
39. M. Yuan *et al.*, A highly conserved cryptic epitope in the receptor binding domains of SARS-CoV-2 and SARS-CoV. *Science* **368**, 630–633 (2020).
40. J. Lan *et al.*, Structure of the SARS-CoV-2 spike receptor-binding domain bound to the ACE2 receptor. *Nature* **581**, 215–220 (2020).
41. S. F. El-Mashtoly *et al.*, Structural changes during the photocycle of photoactive yellow protein monitored by ultraviolet resonance Raman spectra of tyrosine and tryptophan. *J. Phys. Chem. B.* **109**, 23666–23673 (2005).
42. H. Takeuchi, UV Raman markers for structural analysis of aromatic side chains in proteins. *Anal. Sci.* **27**, 1077 (2011).
43. M. Morháč, An algorithm for determination of peak regions and baseline elimination in spectroscopic data. *Nucl. Instrum. Methods Phys. Res. Sect. A: Accelerators, Spectrometers, Detectors and Assoc. Equip.* **600**, 478–487 (2009).
44. M. Holzweber *et al.*, Principal component analysis (PCA)-assisted time-of-flight secondary-ion mass spectrometry (ToF-SIMS): A versatile method for the investigation of self-assembled monolayers and multilayers as precursors for the bottom-up approach of nanoscaled devices. *Anal. Chem.* **86**, 5740–5748 (2014).
45. A. Ditta *et al.*, Principal components analysis of Raman spectral data for screening of Hepatitis C infection. *Spectrochim. Acta Part A Mol. Biomol. Spectr.* **221**, 117173 (2019).